Materials Today Communications 45 (2025) 112423

Contents lists available at ScienceDirect

Materials Today Communications

journal homepage: www.elsevier.com/locate/mtcomm

Macroscopic simulation of hydrogen diffusion across the grain-boundary networks in cold-sprayed Ti6Al4V

Bo Ching Wong [a,b], M.W. Fu [a,*]

[a] Department of Mechanical Engineering, Research Institute for Advanced Manufacturing, The Hong Kong Polytechnic University, Hung Hom, Kowloon, Hong Kong
[b] The Aviation Services Research Centre, The Hong Kong Polytechnic University, Hung Hom, Kowloon, Hong Kong

ARTICLE INFO

Keywords:
Cold spray
Grain-boundary network
Hydrogen diffusion
Hydrogen mitigation
Special boundaries

ABSTRACT

Hydrogen embrittlement in metallic parts is a critical safety risk in the systems and processes involving hydrogen. Cold spray is a trending solid-state additive repair technique that may repair hydrogen degraded components in future, and hydrogen is also considered a carrier gas for the cold spray process. There is a lack of hydrogen diffusion prediction methods for cold-sprayed deposits since their irregular microstructures are formed by the supersonic impact of particles. This paper presents the image-based realistic modelling and hydrogen diffusion simulation with a grain-boundary network approach on cold-sprayed Ti6Al4V microstructure with heat treatments at 540°C and 750°C. Grain boundaries with a misorientation angle of less than 15° in EBSD mapping are categorized as special boundaries, or else the boundaries are random. The simulation is conducted by utilizing the accessible MATLAB Im2mesh tool and ABAQUS to obtain repeatable results. The high fraction of special boundaries in cold-sprayed deposits due to particle deformation has shown its potential as a grain boundary engineering method to improve hydrogen resistance. Dense special boundaries trap hydrogen and overcome the "short-circuit diffusion effect" by random boundaries. Heat treatment induces recrystallization and reduces the fraction of special boundaries, and consequently deteriorates the performance of hydrogen mitigation. The simulation results reveal that the accuracy highly depends on the quality of EBSD characterization and the experimentally measured hydrogen properties. The image-based framework demonstrates its capability to simulate 2D diffusion across the complicated GB network of cold-sprayed deposits, as well as using GB maps from literature despite the raw EBSD data is not provided. This paper aims to provide insights into understanding hydrogen diffusion behaviour in grain-boundary networks and develop techniques to predict the hydrogen-affected zone over the service life of components.

1. Introduction

HE in metal is recognized as a concern for degradation in multiple disciplines, such as the manufacturing and energy industries. The transport of hydrogen atoms is challenging to characterize due to the small size of hydrogen atoms and the perplexing relationship with microstructural features [1]. Since access to advanced hydrogen characterization instruments is costly and limited, the influence of interested microstructural features on hydrogen diffusion is usually studied with synthetic models and FEM simulation [2–6]. However, some irregular microstructures are difficult to mimic, so it would be more practical for metallography engineers to predict the hydrogen-affected zone over the service life with realistic models.

Cold spray has recently aroused research interest in speedily repairing damaged or degraded parts. The HE-susceptible phase change is prevented as the spraying temperature is below the melting point of feedstock powder. This additive technology is a rapid metal deposition technique that features refined polycrystalline microstructure due to the supersonic impact and viscoplastic deformation of particles. Consequently, the extreme cold work on particles leads to poor ductility of deposits [7], where HE would not be a prioritized concern. Post-spray heat treatments are commonly used to recover the ductility of cold-sprayed deposits and assure the serviceability of repaired parts

---

Abbreviations: CSL, coincidence site lattice; EBSD, electron backscatter diffraction; GB, grain boundary; GND, geometrically necessary dislocations; HAGB, high angle grain boundary; HE, hydrogen embrittlement; IPB, interparticle-boundary; LAGB, low angle grain boundary; ROI, region of interest; THP, thermo-hydrogen processing; TJ, triple junctions.

* Correspondence to: Department of Mechanical Engineering, Research Institute for Advanced Manufacturing, The Hong Kong Polytechnic University, Hung Hom, Kowloon, Hong Kong, China.

E-mail address: mmmwfu@polyu.edu.hk (M.W. Fu).

https://doi.org/10.1016/j.mtcomm.2025.112423
Received 13 February 2025; Received in revised form 26 March 2025; Accepted 1 April 2025

Nomenclatures

Σ	coincidence site lattice index
ϕ	normalized concentration
θ	temperature
θ^z	absolute zero temperature
c	hydrogen concentration
c_0	initial hydrogen concentration
c_s	surface hydrogen concentration at the infinite end
D	hydrogen diffusivity
D_g	hydrogen diffusivity in grains
d_{CE}	circle equivalent diameter of grains
$\mathbf{J}$	hydrogen diffusion flux
κ_p	pressure stress factor
κ_s	Soret effect factor
p	partial pressure
s	hydrogen solubility
t	time
x	distance in x-direction

[7–11]. Some of these parts would be employed in environments with hydrogen exposure [12–19], utilizing THP to refine the microstructure further [20,21] or even using hydrogen as cold spray carrier gas [22]. However, the mass transport and hydrogen interaction properties of the cold-sprayed deposits and their microstructure after heat treatments have not been a concern compared to other commercialized additive counterparts to date [23–25].

The GB network is a significant feature for evaluating the hydrogen diffusion mechanism across cold-sprayed deposits on a macroscopic scale. Ichimura et al. [26] found there was a GB cross-effect, where large grain size enhanced diffusion along GB while small grain size suppressed the diffusion by trapping hydrogen at GB junctions. The simulation by Jaseliunaite et al. [6] claimed that diffusion in a polycrystalline GB network was accelerated depending on the morphological features (typical solid, bi-modal, and semi-lamellar), but the potential role of GB as a hydrogen trap was not considered. Since the correlation between GB diffusivity and GND density would be invalid for misorientation $> 15^\circ$ with a complex GB network, Oudriss et al. [27,28] proposed the approach of CSL index for a wide misorientation range. GB were categorized into low misorientation ($\Sigma1$) and special boundaries ($\Sigma3^n < 29$) which trap hydrogen atoms and suppress further diffusion, as well as high-angle random boundaries ($\Sigma > 29$) accelerate the hydrogen diffusion with “short-circuit diffusion effect”. Hoch et al. [2] developed a 2-D model with three phases (grains, special and random boundaries) to study the influence of the GB network towards the effective hydrogen diffusivity. The model was improved to a 3-D continuum network, but some features like TJ were still under investigation to further advance the simulation accuracy [29]. Adair and Johnson [30] used spectral descriptors to compare the diffusion through the synthetic GB networks with different cluster lengths and morphologies, then implemented into the realistic models generated from the EBSD data of Ni in reference and GB engineered states by Randle et al. [31]. The results showed the diffusion in both reference and GB engineered Ni being dominated by HAGB, even though the fractions of LAGB and $\Sigma3$ GB were at least 50 %. Conversely, the diffusion through grains and the solubilities of the GB were not considered. Li et al. [19] suggested the high fraction of special boundaries in the cold-sprayed pure Cu could improve the localized corrosion resistance in used nuclear fuel containers, where the grain size effect on corrosion resistance would be negligible. Hence, the special boundaries in cold-sprayed deposits are key study objectives in GB engineering to resist corrosion, HE and other metal degradation mechanisms.

In addition to the effective hydrogen diffusivity, the hydrogen solubility and the mode of diffusion are essential to assess the hydrogen transport behaviour and affected zone in metals [32]. Hanson et al. [33] attempted to describe the capability of GB blocking chemical transport with the degree of hindrance in synthetic models of solid oxide fuel cell and nickel manganese cobalt cathode, which indeed could be represented by solubility. The GB networks of cold-sprayed deposits exhibited localized refined grains at IPB, which evolved into different phases depending on the heat treatment parameters [7–11]. Thus, heat treatment of cold-sprayed deposits has to be under the phase change temperature if HE is a concern in the employing environment. The hydrogen diffusion behaviour in cold-sprayed deposits with the GB network approach highly depends on the following points: (1) the hydrogen diffusivity and solubility of grains and boundaries, and (2) the ratio of grains to random and special boundaries after different heat treatments.

This study implemented the GB networks approach with realistic 2-D models to investigate the hydrogen diffusion across the cold-sprayed deposits at the stress-relieved phase and recrystallized phase after heat treatment. The GB network approach with image-based modelling simplifies the simulation of hydrogen diffusion across the irregular microstructure in cold-sprayed deposits. Firstly, the EBSD characterized GB maps were converted into realistic models, where the proportions of grains, random and special boundaries were also quantified. Secondly, the diffusible hydrogen concentration maps revealed the hydrogen diffusion behaviour in cold-sprayed deposits and the influence of varying the fraction of random and special boundaries. Thirdly, imaginary scenarios were compared with as-characterized GB networks and examined the mechanism to improve hydrogen resistance. Finally, the limitations in modelling, simulation and implementation in real-world engineering were also discussed. The simulation procedures and results in this work help create the synergy between hydrogen resistance and other properties of cold-sprayed deposits.

2. Methodology

2.1. Sample preparation

Two realistic microstructural 2D models of cold-sprayed Ti6Al4V were constructed from two GB maps. The particle size of feedstock Ti6Al4V powder was about 45 μm (PG-AMP-1120, Plasma Giken, JP). The propellant gas was helium at 900 °C and 3 MPa. A glass-nozzle was used to prevent clogging and powder feeder instability. Stand-off distance was maintained at 25 mm from the CP-Ti substrates. The nozzle was traversing at a constant speed of 1 m/s. The toolpath was a snake scan pattern from top to bottom with a vertical step of 1 mm. The cold-sprayed Ti6Al4V coatings underwent 2 h of 540°C post-spray stress relieving (SR-GB) and 2 h of 750°C post-spray heat treatment (HT-GB), respectively. As-sprayed deposits with helium carrier gas could not be indexed by EBSD due to the presence of ultra-fine grains [34], and thus omitted in this study.

2.2. Characterization

A semi-automatic grinder polisher (Abramin, Struers, DK) was used with SiC paper progressively from 220 down to 4000. Samples were then polished with MD-Chem/OP-S solution (260 ml OP-S: 40 ml H2O2: 1 ml HNO3: 0.5 ml HF) from 50 N down to 12.5 N progressively. The samples underwent argon ion milling (IM4000II, Hitachi, JP) for a smoother surface. Their GB maps were characterized by an EBSD camera (Velocity Super, EDAX, US) installed on SEM (Apreo 2 C, Thermo Fisher Scientific, US). The scanning step sizes were 30 nm and 100 nm for SR-GB and HT-GB, respectively. The GB was categorized by defining LAGB as special boundaries if misorientation $< 15^\circ$ and HAGB as random boundaries if misorientation $> 15^\circ$.

When the misorientation exceeds the threshold angle of 10–15°, the grain-boundary energy would become independent of misorientation due to tight dislocation spacing and overlapping of dislocation cores

[35]. Although the CSL index could be used to further distinguish between random and special HAGB [19], the Σ1 LAGB would have sufficiently high fraction to show the location of special boundaries. Furthermore, there would be more hydrogen properties of the GB with various CSL indices to be assigned without an experimental database. Thus, this simulation only categorized the GB into special LAGB and random HAGB for brevity.

2.3. Modelling

The meshing workflow is illustrated in Fig. 1. The resolution of GB maps was 1200 × 1200 pixels. The images were converted to B&W scale by Windows Photo app and then stacked to RGB by ImageJ [36]. The pre-processed images were meshed into triangular elements by MATLAB add-on im2mesh developed by Ma [37]. The im2mesh input parameters are listed in Table 1. The close-up of the mesh in the centre of Fig. 1 showed the elements of random boundaries being assigned at the junctions rather than categorizing them as individual phases. The input scales refer to the ratio of the side length (μm) in the GB maps to the number of pixels in the corresponding images, where the output mesh parameters are summarized in Table 2. The quantity ratio of special to random boundaries in SR-GB and HT-GB samples were 1.92 and 2.63, respectively. This matched the trend of increased random boundaries and reduced special boundaries due to annealing recrystallization [19, 38]. The multi-section mesh files were then imported into ABAQUS for simulating transient hydrogen diffusion with the following constitutive equation [39–41]:

$$\mathbf{J} = -s\mathbf{D} \bullet \left[\frac{\partial \phi}{\partial x} + \kappa_s \frac{\partial}{\partial x}(\ln(\theta - \theta^z)) + \kappa_p \frac{\partial p}{\partial x}\right] \tag{1}$$

The normalized concentration ϕ is defined as [41]:

$$\phi \frac{c}{s} \tag{2}$$

Since the simulation only considered concentration, the temperature and pressure variables were removed. Thus Eq. (1) was reduced to Fick's first law in its most common form:

$$\mathbf{J} = -s\mathbf{D} \bullet \left(\frac{\partial \phi}{\partial x}\right) = -\mathbf{D} \bullet \frac{\partial c}{\partial x} \tag{3}$$

The continuity equation represented the change of hydrogen concentration in 2D with respect to diffusion time [42]:

$$\frac{\partial c}{\partial t} = -\frac{\partial J}{\partial x} \tag{4}$$

Substituting Eq. (3) into Eq. (4) obtained Fick's second law in 2D:

$$\frac{\partial c(x,y,t)}{\partial t} = \mathbf{D} \bullet \left(\frac{\partial^2 c(x,y,t)}{\partial x^2} + \frac{\partial^2 c(x,y,t)}{\partial y^2}\right) \tag{5}$$

The quantitative analysis of grain size was performed with MATLAB Manual Grain Size Measurement Tool developed by Buchely [43] to overcome the difficulties of grains recognition with automatic programs, as presented in Table 3 and Fig. S1. Oudriss et al. [27] showed the diffusivities of grains in 0.05–5 μm would be in the same order of magnitude, where Li et al. [19] stated the grain size effect on corrosion resistance would be negligible if there were not much nanograins. Thus, the hydrogen properties of grains in all sizes were assumed to be identical for brevity. Since there was a lack of reference about the hydrogen properties of cold-sprayed Ti6Al4V and its grain boundaries at various temperatures, the analogous material parameters were retrieved from

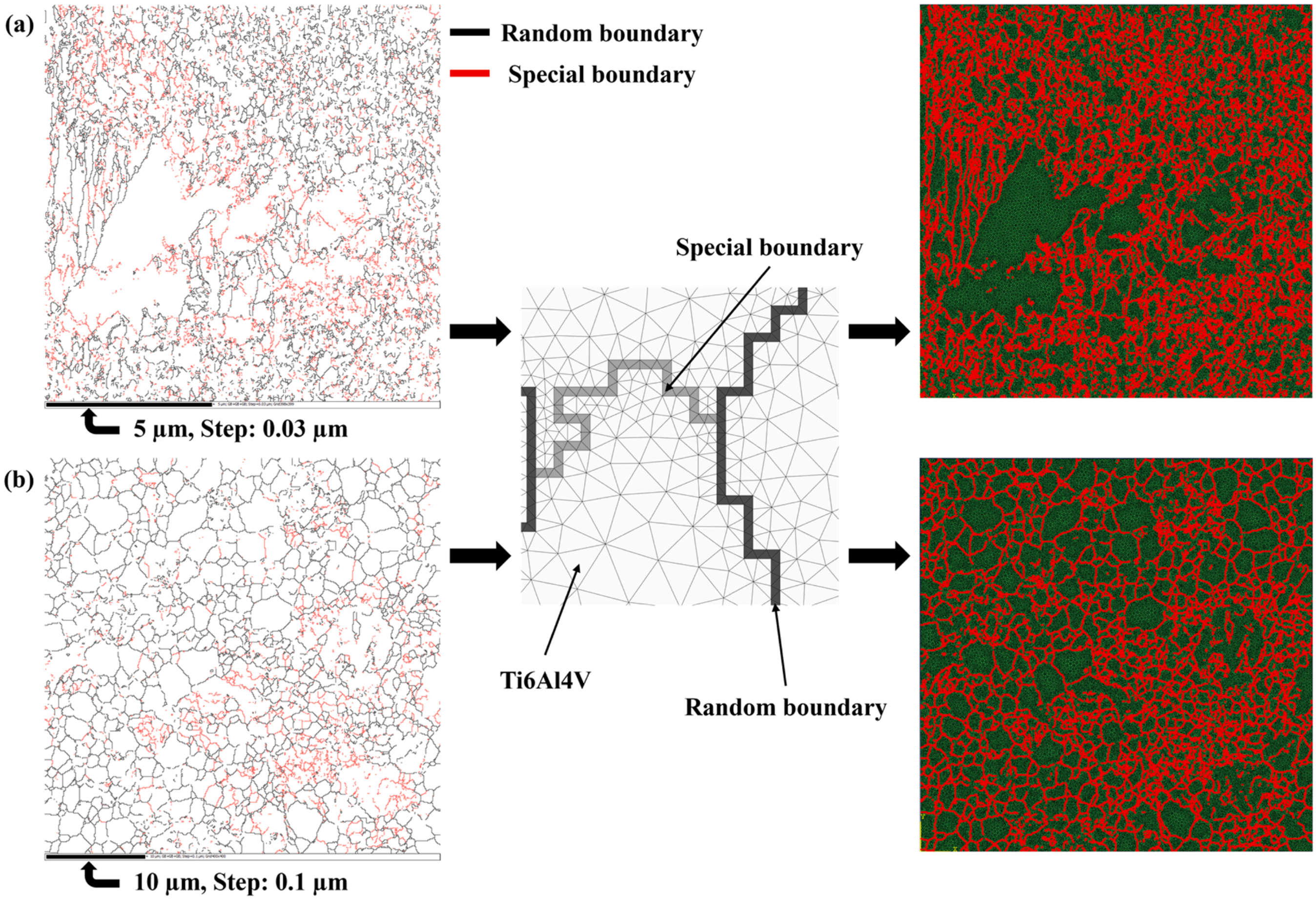

Fig. 1. Meshing from the GB maps of cold-sprayed Ti6Al4V deposits with (a) 540°C post-spray stress relieving and (b) 750°C post-spray heat treatment.

Table 1
Im2mesh input parameters.

Tolerance	Max mesh size h_{max}	Mesh kind	Scalar gradient limit	Scale	Element order	Element type	Precision of node coordinates
Eps	10	Delaunay	+ 2	(a) 0.01 (b) 1/30	1	CPS3	8

Table 2
Output mesh parameters.

Output Mesh Parameters	(a) SR-GB	(b) HT-GB
Total number of nodes	360209	275614
Total number of elements	718368	549583
Number of random GB elements	123101 (17.1 %)	101390 (18.4 %)
Number of special GB elements	63644 (8.9 %)	38566 (7.0 %)
Number of Ti6Al4V-grain elements	531623 (74.0 %)	409627 (74.5 %)

Table 3
Grain Size Measurement.

Statistics	SRGB	HTGB
Number of grains measured	406	400
Max d_{CE} (μm)	5.5346	7.3410
Min d_{CE} (μm)	0.0391	0.4442
Mean d_{CE} (μm)	0.4236	1.7424
STD d_{CE} (μm)	0.3880	0.8933

the relevant studies of Ti6Al4V and GB network measured by electrochemical method at room temperature [2,44,45], as listed in Table 4. Fick's law was selected when the diffusion properties of materials were defined. The units were converted to μm scale. The influence of the β phase was neglected since the processes of cold-spraying and heat treatment were below the phase change temperature of Ti6Al4V [46]. The solubility of grain boundaries was assumed to be 10 % of that of the bulk [47]. Since the hydrogen solubilities were defined manually, Sievert's law was not applicable to the relationship between concentration and partial pressure of hydrogen in this case. The element type was standard linear heat transfer triangle DC2D3. The absolute zero temperature was set as 0. The time increments were 0.01, 0.1 and 1 h depending on the duration of diffusion time. The boundary condition assigned a normalized mass concentration of 500 ppm along the left edge of the model. No boundary condition was defined on the right edge of the model since the boundary with zero concentration should be infinitely far.

The simulation was verified by comparing the numerical results of the monocrystal scenario (time increment of 0.1 h) with the 1D analytical results of Fick's second law [6]:

$$\frac{\partial c(x,t)}{\partial t} = D_g \frac{\partial^2 c(x,t)}{\partial x^2} \tag{6}$$

The model was considered a semi-infinite object with a constant concentration of hydrogen diffusion from one side to the other. The initial and boundary conditions were set as [48]:

$$\mathrm{I.C.}: \mathrm{At}t = 0, c = 0 \tag{7}$$

$$\mathrm{B.C.} \quad 1: \mathrm{At}x = 0, c = c_0 \tag{8}$$

$$\mathrm{B.C.} \quad 2: \mathrm{At}x = \infty, c = c_s = 0 \tag{9}$$

Where c_0 was defined as 1050 ppm in analytical calculation, which was equaled to the solution of Eq. (2) by substituting $\phi = 500$ ppm and $D_g = 2.1$. The solution of Eq. (6) became [48]:

$$c(x,t) = c_0 \mathrm{erfc}\left(\frac{x}{2\sqrt{D_g t}}\right) \tag{10}$$

Where the complementary error function was:

$$\mathrm{erfc}(x) = 1 - \frac{2}{\sqrt{\pi}} \int_0^x e^{-t^2} dt \tag{11}$$

Table 4
Material parameters in ABAQUS.

Materials	Diffusivity ($\mu m^2/h$)	Concentration (ppm)	Solubility ($ppm*\mu m*N^{-1/2}$)	References
Ti6Al4V	12.6	0	2.1	[44,45]
Special GB	0.36	0	0.21	[2,47]
Random GB	360,000	0	0.21	[2,47]

It was noted that the real hydrogen diffusivity of a single Ti6Al4V crystal should be higher due to the absence of micro-defects as hydrogen trapping sites according to the GB cross-effect [26], which would drastically reduce the actual saturation time. Therefore, the monocrystal scenario was only used as a reference to verify the confidence of model implementation and examine the effect of the GB network on diffusion.

There were 1000 evenly spaced points along the true distance of SR-GB (12 μm) and HT-GB (40 μm) models in the analytical solution. Fig. 2**a & b** show the concentration maps of the monocrystal scenario in SR-GB and HT-GB, respectively, by assigning grain properties to the GB elements. The simulation step time was 50 h with an increment of 0.1 h. Their analytical and numerical diffusion profiles are presented in Fig. 2**c & d**. The settings of a linearly spaced vector did not induce any change to analytical values. Both solution results had good curve fitting for time instances of 0.1 h, 0.5 h and 1 h. However, the numerical result concentrations at the end of model SR-GB (Fig. 2**c**) were about 300 ppm higher than those of analytical starting from t = 5 h to 50 h. On the other hand, the analytical and numerical results in the model HT-GB (Fig. 2**d**) still aligned with each other for t = 5 and 10 h, although the disparity of about 300 ppm appeared for t = 50 h. It was not surprising that the analytical and numerical results differ for extensive step time with cumulative disparity [49]. However, the time instances of disagreement depended on the true distance scales as the element sizes of models [50]. An image of a German flag with dimensions of 1600 × 959 pixel was converted into 12 μm and 40 μm wide models with scales of 3/400 and 1/40, respectively. The number of elements in both models was 73335. The same diffusion simulation of the monocrystal scenario was performed with the two German flag models (Fig. S2), where the same diffusion profiles in Fig. 2**c & d** were obtained. These results had proved that the model with a longer true distance provides higher confidence in model implementation, where the morphology of the mesh structure did not affect significantly.

This was because of the effect of finite domain boundaries in ABAQUS becoming significant over a prolonged period and deviating from the idealized semi-infinite domain solution. Increasing the size of the finite domain in ABAQUS could better match the semi-infinite domain, that explained the finite model with a longer true distance delaying the time of deviation from the semi-infinite one. However, the size of the finite domain could not be changed as it depended on the true distance in the SEM/EBSD image. Introducing infinite elements in ABAQUS might better align with the analytical semi-infinite solution, which would need further study to debug the errors and ensure the validity of boundary condition settings. Moreover, verifying with other numerical solvers might also help check whether the deviation issue was specific to

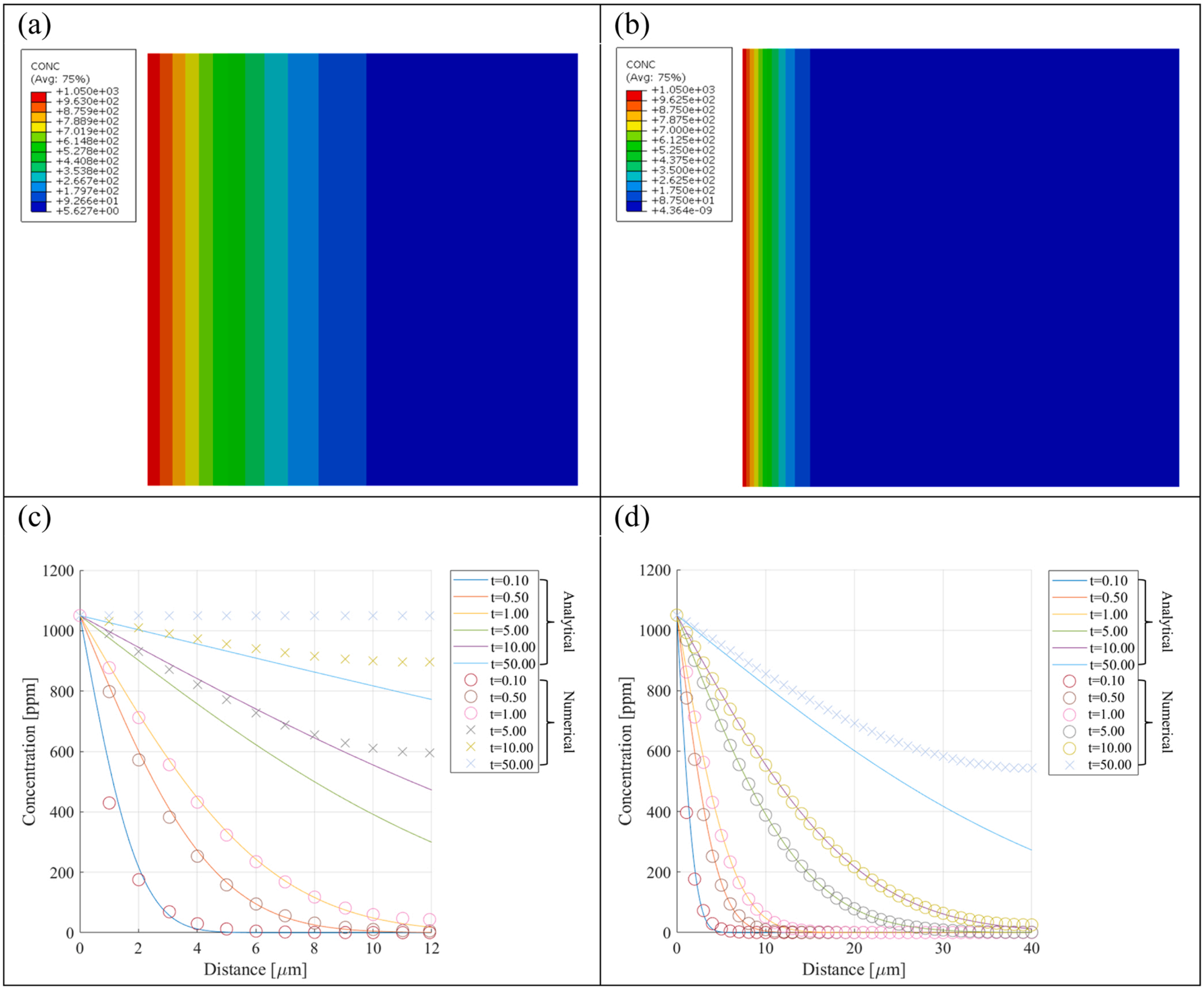

Fig. 2. Hydrogen concentration maps in numerical simulations of (a) SR-GB and (b) HT-GB monocrystal at t = 0.5 h. Comparison of analytical and numerical hydrogen diffusion profiles in monocrystal scenario of (c) SR-GB and (d) HT-GB.

ABAQUS or consistent across numerical solvers. It was noted that importing the im2mesh output INP files into other FEM software like ANSYS might result in wrong scales, which would need extra calibration.

3. Results and discussion

3.1. Diffusion across GB networks after heat treatments

The simulation results with time increment of 0.01 h are shown in Fig. 3. The hydrogen flux in both samples had already displaced 3–5 μm from the high concentration surface after 0.1 h of diffusion. The diffusion periods to obtain a near saturation state were about 7.72 h and 25.01 h for SR-GB and HT-GB, respectively. The videos of evolving concentration maps are included in the supplementary files **Vid. S1 & 2.** Bulk (lattice) diffusion was dominant in both samples, which was reasonable as the grain elements were about 74 % of the total number of elements. A more tortuous diffusion was observed in HT-GB. Its range of grain size was mostly 1–5 μm, where the true overall width of the micrograph was 40 μm. In contrast, the SR-GB contained mostly 0.1 μm grains and a 6 μm bulk grain across the true overall width of 12 μm, where the evolution of diffusion contour was relatively parallel. In other words, there is an optimum ratio of grain size to micrograph width (1:40–1:8 in this study) to observe a tortuous diffusion. However, the tortuosity of GB network did not show notable differences in terms of diffusion speed in macroscopic observations. The hydrogen diffusion was slower in the monocrystal Ti6Al4V than those in both as-characterized GB networks when the same value of hydrogen diffusivity was assigned. The GB network with the majority of random GBs provided straight pathways for hydrogen diffusion [51]. The straight pathways were removed in the monocrystals so, of course, the diffusion was mitigated.

The close-up in Fig. 3**a & f** also showed the random boundaries breaking through the clusters of special boundaries and thus weakened its blockage effect [2]. The hydrogen diffusion was only barricaded at a few locations, and then the special boundaries were circumvented soon by hydrogen which diffused through the grains and random boundaries. The details of diffusion between grain, random and special boundaries were further illustrated with the German flag models in Fig. S3 **& 4.** The small proportion and discontinuity of special boundaries were the main reasons the GB network model in both samples failed to mitigate hydrogen diffusion, which agreed with the observation by Adair and Johnson [30].

To further examine the impact of the GB network on the hydrogen

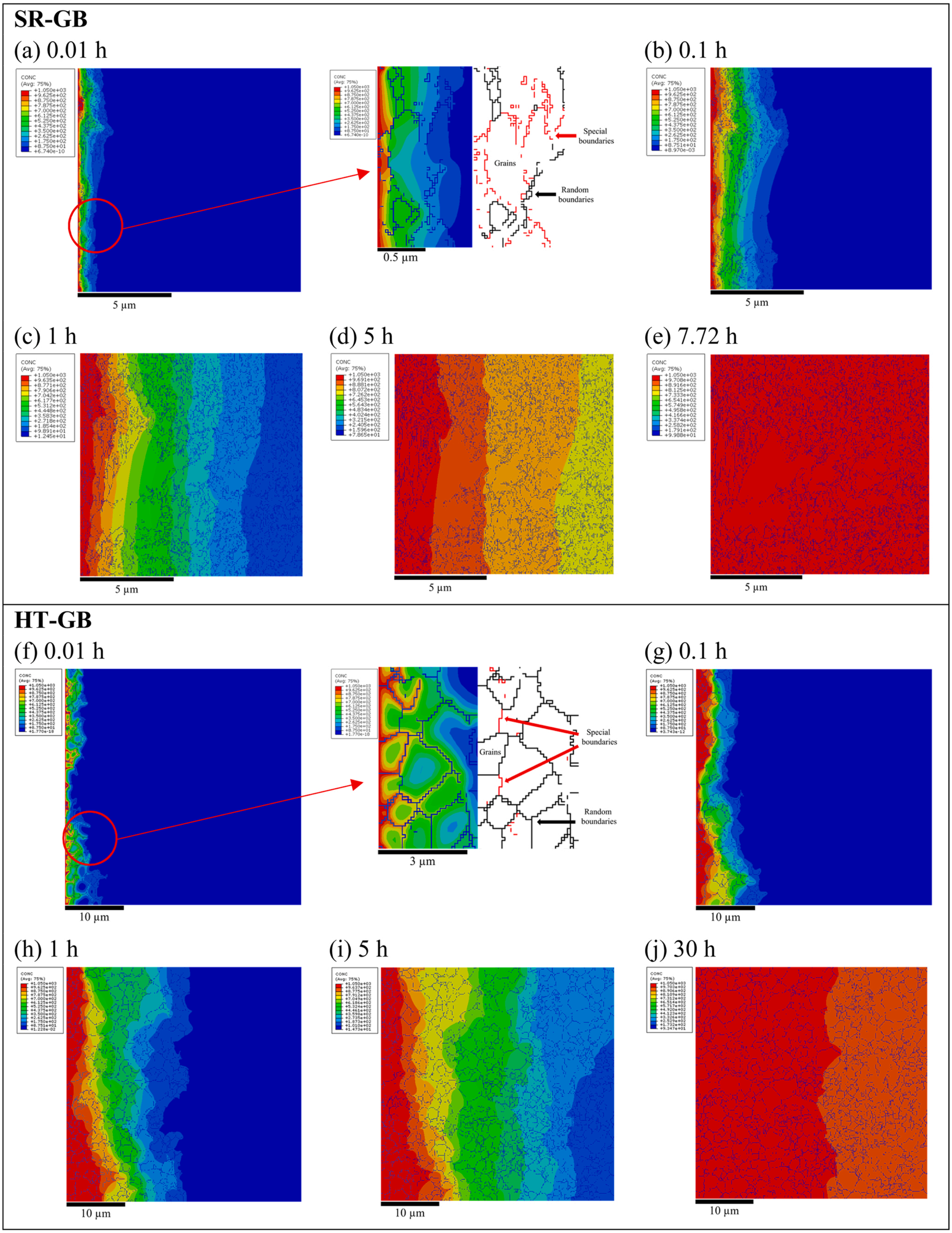

Fig. 3. Simulated hydrogen concentration maps across the as-characterized GB networks of cold-sprayed Ti6Al4V deposits with (a-e) 540°C stress relieving and (f-j) 750°C heat treatment at the marked time instances. Close-ups of ROIs in (a & f) were matched with their corresponding GB maps.

diffusion, the hydrogen diffusion profiles along the displacement of the horizontal centerline in the models were plotted in Fig. 4. In general, the diffusion in SR-GB was smoother than that in HT-GB throughout different time periods. The GB contributed to instantaneous low hydrogen concentration in a discrete pattern, but the hydrogen concentration rebounded to the previous level once circumventing the GB. The sharp concentration drops in SR-GB (at 1.6–1.8 μm) and throughout HT-GB were due to hydrogen dissolving in bulk grains. In contrast, the hydrogen concentration descended steadily across the submicron grains. This was aligned with the aforementioned relationship between tortuous diffusion patterns and the ratio of grain size to micrograph width. However, the relationship between the tortuosity of the diffusion pathway and diffusion speed could not be compared fairly since the models were meshed from source images with the same pixels but different true dimensions. Hence, the following section compares the diffusion of the same models with different ratios of grains to random and special boundaries.

The previous simulation with analogous parameters only resulted in bulk-dominant diffusion. Imaginary ratios of grains to random and special boundaries were set to estimate the conditions of other diffusion modes [32]. Properties of both special and random boundaries remained the same in the first two scenarios. The diffusivity and solubility of the Ti6Al4V grain were only changed in the last GB diffusion scenario.

3.2. *Comparison with diffusion in whole-random boundaries*

The first scenario was replacing the special boundaries with random boundaries, as shown in Fig. 5a & c. The quantity ratio of random boundaries to grains in SR-GB changed from 8.31 to 2.85, and that in HT-GB changed from 10.57 to 2.9. HT-GB exhibited similar trends to its original counterpart. There were dense special boundaries at the lower half of HT-GB originally in Fig. 1b, blocking partial hydrogen diffusion through the region. The original high-concentration locations at the upper half were redirected to the lower half when the special boundaries became random boundaries, where the diffusion displacement was 2–4 μm ahead at t = 1 h. On the other hand, the previously discrete pattern in SR-GB (Fig. 4a) became continuous with about 200 ppm higher concentration (Fig. 5a), which was due to the increased connectivity of GB. Furthermore, this also reflected the special boundaries only had the extremely limited effect of mitigating the diffusion in the original scenario. In other words, the hydrogen traps were too little to overcome the short-circuit diffusion as the fraction of special boundaries was half of the random boundaries, which almost equalled the short-circuit diffusion with random boundaries only.

3.3. *Comparison with diffusion in whole-special boundaries*

The second scenario defined all GB as special boundaries, as shown in Fig. 6a & c. This remarkably increased the connectivity and blockage effect of special boundaries. The as-characterized SR-GB took 10 h to reach a saturation state (Fig. 4a) but it extended to 35 h with a complete special boundary network (Fig. 6b). The mitigation of hydrogen diffusion was more significant in HT-GB where the concentration at the right boundary reached only 320 ppm after 100 h (Fig. 6d). Although the diffusion scenarios were like surface diffusion illustrated by Yazdipour et al. [32], they were actually bulk diffusion. The low-diffusivity special boundaries segregate neighboring grains, and thus, hydrogen atoms need to circumvent through longer distances. The diffusion tended to proceed to the next grain after a high concentration was reached across the previous grain. The original scenarios were bulk diffusion across the "floodplain," where the enhanced special boundaries network transformed the microstructure into the "detention basins" to mitigate the bulk diffusion. If the hydrogen diffusivity and solubility are substituted with those of the corrosive media in other metals, it might explain the localized corrosion resistance in cold-sprayed metals [19]. The two types of GB should form a connected network in the real world, but the GB clusters were discontinued in the GB maps due to the nature of cold-sprayed hard metal deposits with helium gas [34]. The as-sprayed Ti6Al4V microstructure should have excess special boundaries and achieve hydrogen mitigation without the influence of heat treatment. Hence, the hydrogen trapping behaviours of special boundaries need further study with improved EBSD characterization or processing on the GB maps.

3.4. *Effect of hydrogen properties of β grains*

The last scenario in Fig. 7a & c changed the diffusivity and solubility of Ti6Al4V grains to 1260 $\mu m^2/h$ and 0.021 $ppm^* \mu m^* N^{-1/2}$, respectively. This mimicked replacing the Ti6Al4V grains with TiV in the BCC β phase, which featured higher diffusivity and lower solubility [52,53]. The time increment changed to 0.001 h for a time range of 0–0.1 h due to the fast diffusion. The much lower solubility of grains than those of GB was the key parameter inducing GB diffusion to become the dominant mechanism. The highest concentration was reduced for a scale of magnitude as both random and special boundaries became more soluble than the grains. Jaseliunaite et al. [6] set the GB diffusivity to 10,000 times the grain diffusivity to obtain a GB diffusion across polycrystalline microstructure with solid grains. Still, solubility was not accounted for in that simulation. If the fraction of GB and their properties remained the same as the original scenario, SR-GB would reach a saturation state within 0.2 h (Fig. 7b), and HT-GB would be saturated within 1 h

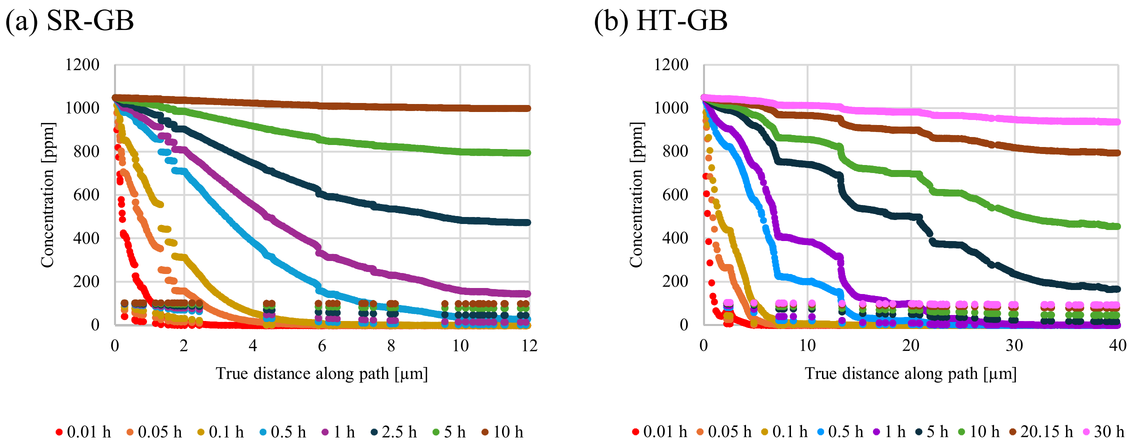
(a) SR-GB (b) HT-GB

Fig. 4. Simulated hydrogen diffusion profiles along the horizontal centerline in the models of cold-sprayed Ti6Al4V deposits with (a) 540°C stress relieving and (b) 750°C heat treatment at various time instances.

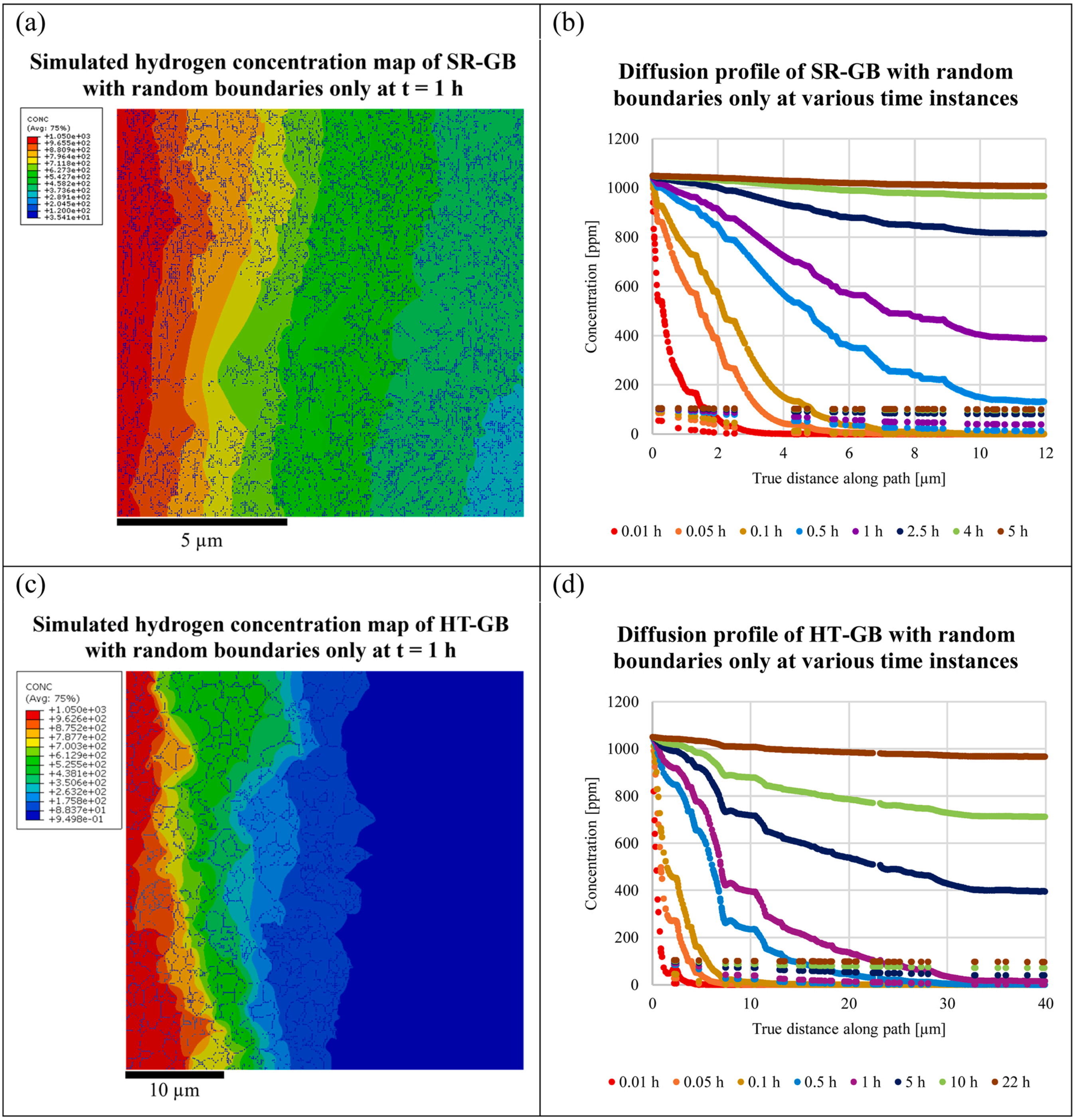

Fig. 5. Simulated hydrogen concentration maps and diffusion profiles of cold-sprayed Ti6Al4V deposits with (a & b) 540°C stress relieving and (c & d) 750°C heat treatment in imaginary conditions containing random boundaries only.

(Fig. 7d). Since hydrogen diffused across the GB network in the initial stage rather than dissolved in the surficial grains and proceeded bulk diffusion like in previous scenarios, the formation of hydrides along the GB network with deep displacement would occur.

3.5. Limitations

The simulation of hydrogen diffusion with the GB network approach highly relies on the quality of EBSD characterization. The cold-sprayed deposits of soft feedstock metal powder with nitrogen or low-pressure helium carrier gas would make it easier to obtain reliable EBSD data [19,54–56]. The dark non-indexed regions in cold-sprayed and highly cold-worked hard metals like Ti6Al4V are inevitable [34,57]. Wang et al. used low-temperature (300°C) annealing to improve the index rate in severely shot peened Ti6Al4V, but its potential influence on submicron structure needs to be considered. In this study, the GB maps did not achieve a continuous GB network even after the heat treatment above 300°C. Despite discontinuous GB structures serving as initiation sites for recrystallization [58], the discontinuous GB network in EBSD characterization of cold-sprayed deposits is more relevant to the step size and grain size.

The simulation procedures and parameters above were implemented

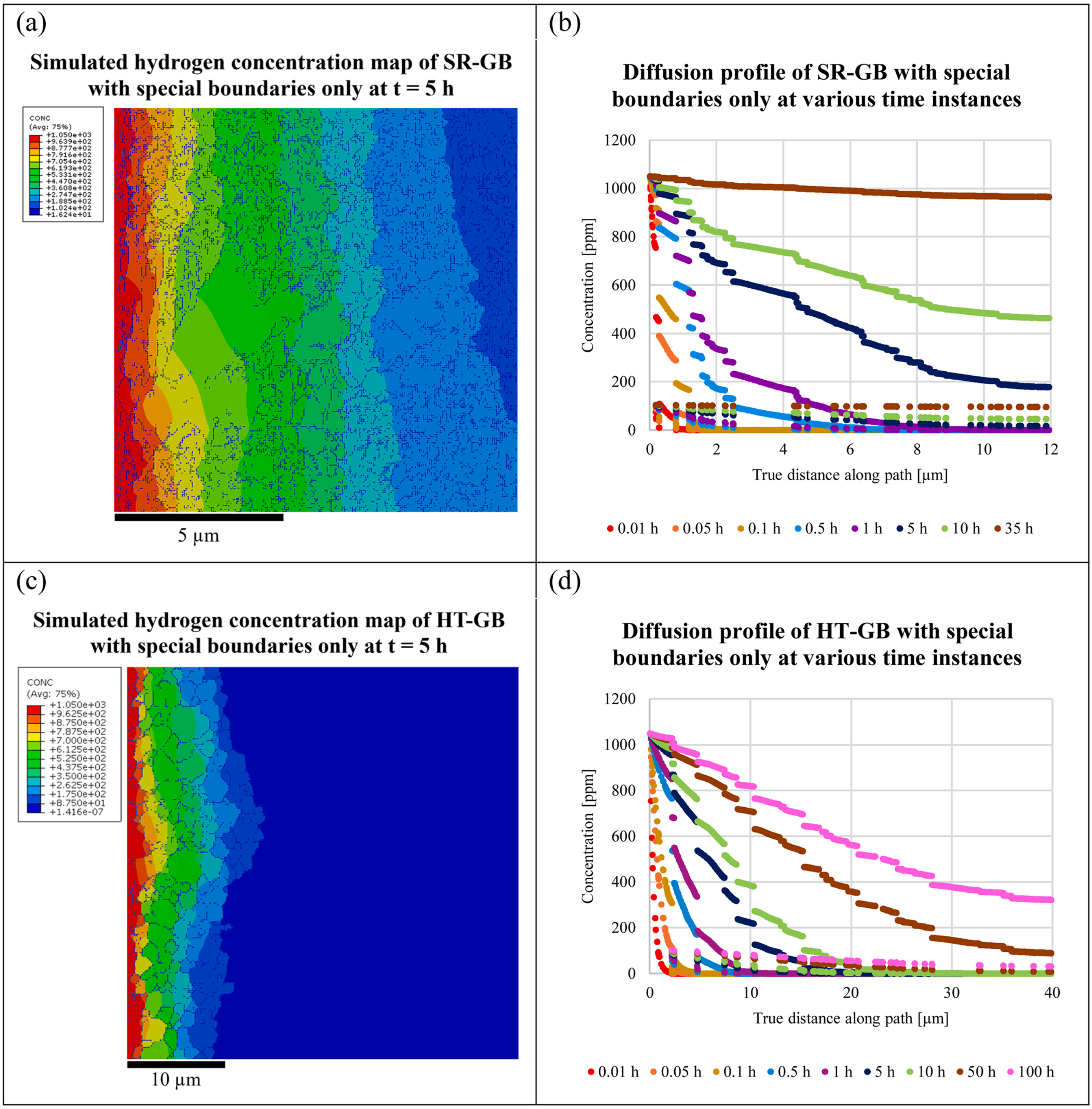

Fig. 6. Simulated hydrogen concentration maps and diffusion profiles of cold-sprayed Ti6Al4V deposits with (a & b) 540°C stress relieving and (c & d) 750°C heat treatment in imaginary conditions containing special boundaries only.

in the well-indexed GB maps of cold-sprayed Al-2Cu and Al-5Cu coatings in the study by Liu et al. [54], where their fractions of LAGB were 55.5 % and 62.8 %, respectively. The true widths of both GB maps were 48 μm wide. The rgb2ind function in MATLAB was used to limit the number of colours to three. Material parameters remained the same as in Table 4. The simulated diffusion rate across the as-characterized Al-Cu GB maps in Fig. 8a-f were similar to those in Ti6Al4V due to excess random boundaries. Still, the diffusion became more tortuous with enhanced connectivity of the GB network. Al-5Cu coating had a slightly slower diffusion rate likely because of the 7.3 % LAGB more than Al-2Cu. The diffusion mitigation became significant in the imaginary scenario with well-connected special boundaries only, as shown in Fig. 8g-l. This demonstrates the connected GB network with a high fraction of special boundaries can mitigate hydrogen diffusion. Contrariwise, it also leads to a low EBSD-index rate and certain brittleness of deposits by such intense grain refinement. Heat treatment is necessary for structural repair, where the hydrogen barrier layer should stay as-sprayed or apply additional surface modification after heat treatment. Anyhow, the cold-sprayed coatings with dense special boundaries make it difficult to obtain reliable GB maps and implement this realistic modelling method. The economic solution would be to join the discontinued GB through image processing, where the assignment of additional random and special boundaries is challenging. In addition, TJs also need to be recognized in image processing as their diffusivity can be triple that of GB and 70 times higher than that of interstitial sites in the case of nanocrystalline Ni [59]. The hybrid modelling methods are

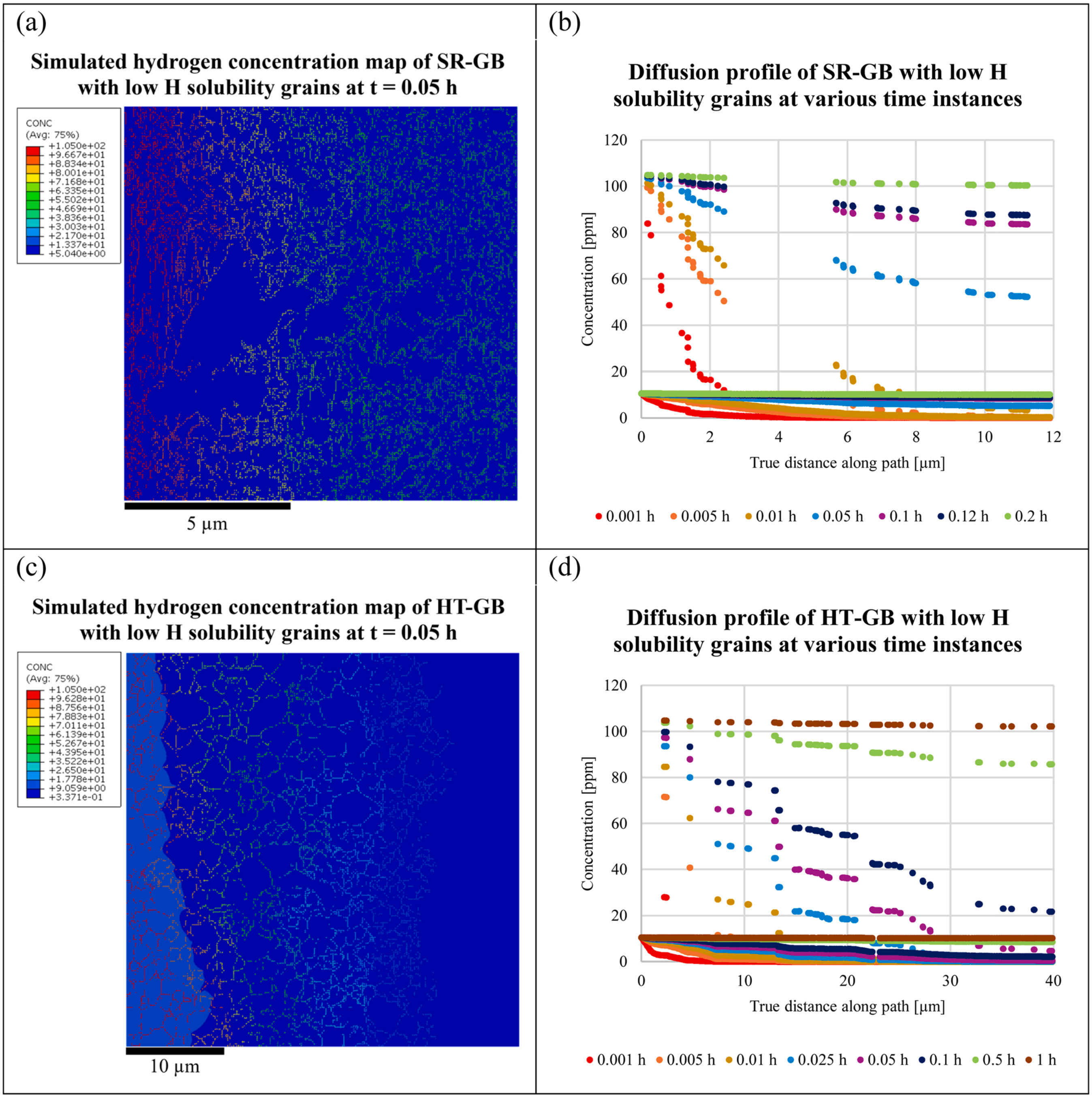
(a) Simulated hydrogen concentration map of SR-GB with low H solubility grains at t = 0.05 h

(b) Diffusion profile of SR-GB with low H solubility grains at various time instances

(c) Simulated hydrogen concentration map of HT-GB with low H solubility grains at t = 0.05 h

(d) Diffusion profile of HT-GB with low H solubility grains at various time instances

Fig. 7. Simulated hydrogen concentration maps and diffusion profiles of cold-sprayed Ti6Al4V deposits with (a & b) 540°C stress relieving and (c & d) 750°C heat treatment in imaginary conditions containing grains with low H solubility.

recommended to comprehend the concerns above and improve the accuracy of hydrogen diffusion simulation across cold-sprayed microstructures. If the CSL indices approach is used to categorize the GB with different misorientations, their corresponding GB energy and hydrogen properties would need extensive study before implementing in the GB network model.

The hydrogen diffusivity and solubility of grains and GB were retrieved from literature, but they were not equivalent to the real hydrogen properties of cold-sprayed Ti6Al4V grains in various sizes and GB with various CSL indices. The im2mesh tool [37] could generate multi-parts model with detailed classification of grains and GB, but the recognition and properties assignment would become extremely complicated in the polycrystalline microstructure like cold-sprayed deposit. Comprehensive simulation for interested metals will require an experimental database like [26,47,51] at various conditions, particularly the hydrogen charging method, temperature and pressure. It is noteworthy that fabricating standardized samples with cold-sprayed Ti6Al4V for hydrogen permeation tests or atomic probe tomography is challenging. The permeation foils and tomography needles bend severely due to the highly deformed microstructure plus the coating nature with biaxial stress. Wire-cutting can lead to surface grain recrystallization and loss of special boundaries by the elevated temperature of electrical current. A layer of brass oxide remains on the cut surface, which needs to be ground away. Furthermore, the contamination of epoxy resin infiltrated into micropores of cold-sprayed deposits leads to unreliable composition analysis, especially since the required

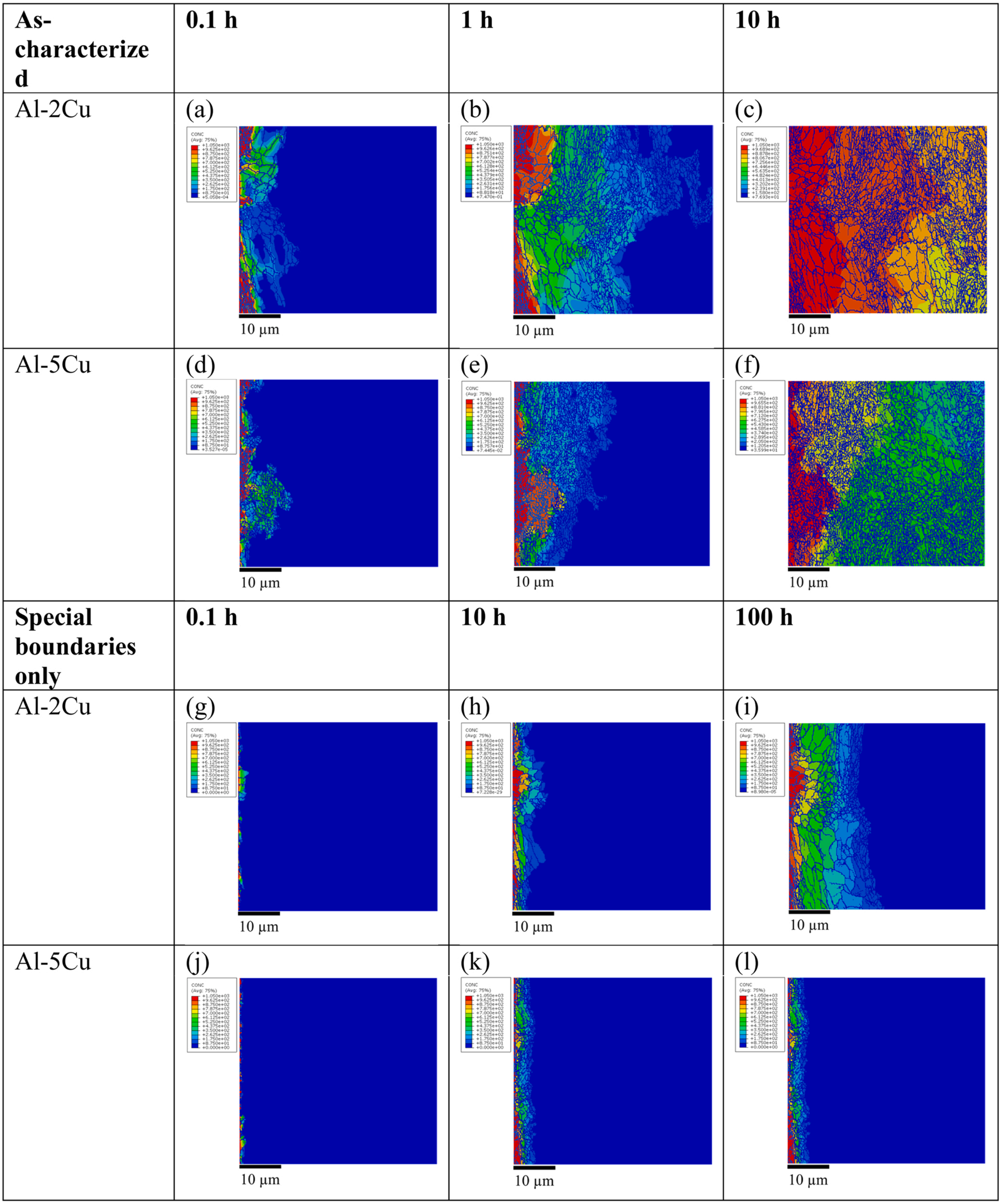

Fig. 8. Simulated hydrogen concentration maps of cold-sprayed (a-c, g-i) Al-2Cu and (d-f, j-l) Al-5Cu deposits in the study of Liu et al. [54] with (a-f) as-characterized GB fractions and (g-l) special boundaries only.

accuracy of hydrogen content characterization is much higher than other bulky elements. Removing epoxy resin with multiple solvents also increases the uncertain influences of hydrogen content on the specimens [60]. Experimental validations remain a challenge unless the limitations above can be resolved.

3.6. Challenges in 3D extension

Reconstructing the 3D GB network models from the 2D models is challenging for cold-sprayed deposits. Murgas et al. [61] attempted generating as-sprayed AA7050 with EBSD maps and the integrated SliceGAN-Dream3D platform. The detailed morphological and crystallographic information of ultrafine and coarse grains were successfully acquired with a step size of 166 nm. SliceGAN was able to generate high-quality binary and three-phase microstructures but could not recognize the GB well in polycrystalline microstructures. Although the SliceGAN-Dream3D was sufficient to simulate micromechanical performance, the GB recognition issue and sampling speed in diffusion models would require extensive study to overcome. For ideal synthetic models, Adair and Johnson [30] extended their diffusivity model to 3D by assigning the boundary conditions on the 2D line to the 3D plane. However, the 3D model was generated with Neper Polycrystal rather than converting the reference and GB engineered Ni models in their 2D analysis, where the GB conversion from 2D EBSD maps to realistic 3D models was not achieved. Implementing this method on cold-sprayed titanium alloys would be even more difficult due to the low EBSD index rate. Sayet et al. [29] compared the normalized effective diffusivity against the change of random boundaries fraction between synthetic 2D and 3D models with varying grain sizes. Both curves in 2D and 3D were exhibited as sigmoid functions with inflection points at 0.5 and 0.3, respectively. The normalized effective diffusivity of the 3D model was always higher than that in the 2D model with smaller nanograins in 20 and 50 nm. However, the disparity in normalized effective diffusivity reduced along with the increase of grain size, where the curve would be flattened if the grains enlarged to microscale. In other words, the difference in diffusivities between the 2D and 3D models are very limited for the cold-sprayed deposits with coarse grains by less deformation or recrystallization heat treatment. Cold-sprayed deposits with severely deformed particles contain grains from nano to microscale can use this relationship to predict 3D localized diffusivity but predicting 3D bulk diffusivity still requires further advance in 3D GB recognition and reduced computation time.

4. Conclusions

This study performed realistic modelling and hydrogen diffusion simulation on a macroscopic scale on the cold-sprayed Ti6Al4V samples after stress-relieving and heat treatment. The experience in this study may provide inspiration for researchers and on-site engineers to further investigate GB engineering in mitigating hydrogen diffusion, predict the hydrogen-affected zone in components, and establish safety standards for cold-sprayed deposits and other GB engineered materials in hydrogen applications. The findings are concluded as follows:

(1) The special boundaries in cold-sprayed deposits need to be abundant enough to trigger its hydrogen trapping ability and overcome the “short-circuit diffusion effect” by random boundaries. The as-characterized SR-GB and HT-GB samples with special to random boundaries ratio of 1.92 and 2.63, respectively, exhibit bulk diffusion across the “floodplain”. On the other hand, the complete special boundaries network in imaginary scenario acts as the “detention basins” to mitigate the bulk diffusion.

(2) The hydrogen mitigation mechanism is elucidated as the low-diffusivity special boundaries segregating neighboring grains which hydrogen atoms need to circumvent for a longer distance with a high concentration across the whole grain before migrating to the next grain. Recrystallization during heat treatment reduces the fraction of special boundaries and thus deteriorates the hydrogen mitigation performance. Additional hydrogen mitigation methods are required if heat treatment on cold-sprayed deposit is compulsory.

(3) The as-sprayed deposits with helium carrier gas cannot be indexed by EBSD due to the presence of ultra-fine grains, which may need prolonged low-temperature annealing to improve the index rate and proceed realistic modelling. Image processing is necessary to aid unrecognizable features like TJ in GB maps. Hydrogen properties of grains and boundaries need to be measured and calculated on a case-by-case basis, whereas measuring hydrogen properties on cold-sprayed deposits is difficult due to problems like specimen bending and composition contamination.

Ethics declaration

Not applicable.

Funding

The setup of the high-pressure cold spray system was part funded by the Hong Kong Government Innovation and Technology Commission (ITC) with the research grant awarded to the HKPolyU Aviation Services Research Centre (ASRC) in collaboration with The Boeing Company and other industrial sponsorship (ITS/075/18FP - Cold Spray Material Deposition). Bo Ching Wong is a PhD student in the HKPolyU Department of Mechanical Engineering (supervised by Prof. M.W. Fu) and conducts research in ASRC (mentored by ASRC engineers).

CRediT authorship contribution statement

Fu M.W.: Writing – review & editing, Supervision. **Wong Bo Ching:** Writing – original draft, Visualization, Validation, Software, Methodology, Investigation, Formal analysis, Data curation, Conceptualization.

Code availability

The software and code used in this study were either open-source or commercially available.

Consent to participate

Not applicable.

Consent for publication

Not applicable.

Declaration of Competing Interest

The authors declare that they have no known competing financial interests or personal relationships that could have appeared to influence the work reported in this paper.

Acknowledgments

The authors would like to thank the staff members in the Aviation Services Research Centre (ASRC), and Industrial Centre (IC), as well as Hong Kong Aero Engine Services Limited (HAESL) and ZKKF (Beijing) Science & Technology Company for their technical support. The setup of the high-pressure cold spray system was part funded by the Hong Kong Government Innovation and Technology Commission (ITC) with the research grant awarded to the HKPolyU Aviation Services Research Centre (ASRC) in collaboration with The Boeing Company and other industrial sponsorship (ITS/075/18FP - Cold Spray Material Deposition).

Appendix A. Supporting information

Supplementary data associated with this article can be found in the online version at doi:10.1016/j.mtcomm.2025.112423.

Data availability

Data will be made available on request.

References

[1] K. Shimizu, K. Nishimura, K. Matsuda, N. Nunomura, T. Namiki, T. Tsuchiya, S. Akamaru, S. Lee, T. Tsuru, W. Higemoto, H. Toda, Novel approach to explore hydrogen trapping sites in aluminum: Integrating Muon spin relaxation with first-principles calculations, Int J. Hydrog. Energy 95 (Dec. 2024) 292–299, https://doi.org/10.1016/j.ijhydene.2024.11.265.

[2] B. Osman Hoch, A. Metsue, J. Bouhattate, X. Feaugas, Effects of grain-boundary networks on the macroscopic diffusivity of hydrogen in polycrystalline materials, Comput. Mater. Sci. 97 (Feb. 2015) 276–284, https://doi.org/10.1016/j.commatsci.2014.10.048.

[3] P. Cavaliere, A. Perrone, D. Marsano, A. Marzanese, B. Sadeghi, Modelling of the hydrogen embrittlement in austenitic stainless steels, Mater. (Oxf.) 30 (Aug. 2023) 101855, https://doi.org/10.1016/j.mtla.2023.101855.

[4] P. Cavaliere, B. Sadeghi, A. Perrone, D. Marsano, A. Marzanese, Modelling of hydrogen diffusion leading to embrittlement in austenitic stainless steels, Int. J. Press. Vessels Pip. 208 (Apr. 2024) 105120, https://doi.org/10.1016/j.ijpvp.2023.105120.

[5] R.F. Schaller, J.R. Scully, Spatial determination of diffusible hydrogen concentrations proximate to pits in a Fe–Cr–Ni–Mo steel using the Scanning Kelvin Probe, Electrochem Commun. 63 (Feb. 2016) 5–9, https://doi.org/10.1016/j.elecom.2015.12.002.

[6] J. Jaseliūnaitė, M. Povilaitis, A. Galdikas, Kinetic Modeling of Grain Boundary Diffusion: Typical, Bi-Modal, and Semi-Lamellar Polycrystalline Coating Morphologies, Coatings 12 (7) (Jul. 2022) 992, https://doi.org/10.3390/coatings12070992.

[7] R. Huang, M. Sone, W. Ma, H. Fukanuma, The effects of heat treatment on the mechanical properties of cold-sprayed coatings, Surf. Coat. Technol. 261 (Jan. 2015) 278–288, https://doi.org/10.1016/j.surfcoat.2014.11.017.

[8] P. Vo, E. Irissou, J.G. Legoux, S. Yue, Mechanical and microstructural characterization of cold-sprayed Ti-6Al-4V after heat treatment, J. Therm. Spray. Technol. 22 (6) (Aug. 2013) 954–964, https://doi.org/10.1007/s11666-013-9945-4.

[9] A.C. Hall, D.J. Cook, R.A. Neiser, T.J. Roemer, D.A. Hirschfeld, The effect of a simple annealing heat treatment on the mechanical properties of cold-sprayed aluminum, *2006 15:2*, J. Therm. Spray. Technol. 15 (2) (Jun. 2006) 233–238, https://doi.org/10.1361/105996306X108138.

[10] L. Yang, S. Wang, X. Luo, P. Wang, H. Yang, H. Li, J. Xiang, X. Bai, Microstructural Nano-Scale Evolution at Inter-Particles Bonding Interface of Cold-Sprayed Ti6Al4V Deposits During Heat Treatment, *2023*, J. Therm. Spray. Technol. (Oct. 2023) 1–16, https://doi.org/10.1007/s11666-023-01671-6.

[11] M. Kazasidis, E. Verna, S. Yin, R. Lupoi, The effect of heat treatment and impact angle on the erosion behavior of nickel-tungsten carbide cold spray coating using response surface methodology, Emergent Mater. 4 (6) (Dec. 2021) 1605–1618, https://doi.org/10.1007/s42247-021-00274-7.

[12] K. Ogawa, D. Seo, K. Ogawa, D. Seo, Repair of Turbine Blades Using Cold Spray Technique, Adv. Gas. Turbine Technol. (Nov. 2011), https://doi.org/10.5772/23623.

[13] Y. Meng, H. Saito, C.A. Bernard, Y. Ichikawa, K. Ogawa, Parametric Study to Repair Leaks in Water Pipe Using the Low-Pressure Cold Spray Technique, J. Therm. Spray. Technol. 31 (8) (Dec. 2022) 2560–2576, https://doi.org/10.1007/s11666-022-01469-y.

[14] V.K. Champagne, The repair of magnesium rotorcraft components by cold spray, J. Fail. Anal. Prev. 8 (2) (Apr. 2008) 164–175, https://doi.org/10.1007/s11668-008-9116-y.

[15] P. Vo, D. Poirier, J.-G. Legoux, E. Irissou, P.G. Keech, Application of Copper Coatings onto Used-Fuel Canisters for the Canadian Nuclear Industry. in *High Pressure Cold Spray*, ASM International, 2016, pp. 253–276, https://doi.org/10.31399/asm.tb.hpcspa.t54460253.

[16] C.H. Boyle, S.A. Meguid, Mechanical performance of integrally bonded copper coatings for the long term disposal of used nuclear fuel, Nucl. Eng. Des. 293 (Nov. 2015) 403–412, https://doi.org/10.1016/j.nucengdes.2015.08.011.

[17] M. Ialovega, T. Dabney, M.N. Gonzalez, H. Yeom, D. Velez, E. Willing, J. K. Anderson, T. Angot, R. Bisson, C. Forest, A. Kreter, O. Schmitz, K. Sridharan, Initial study on thermal stability of cold spray tantalum coating irradiated with deuterium for fusion applications, Phys. Scr. 98 (11) (Oct. 2023) 115611, https://doi.org/10.1088/1402-4896/ad0098.

[18] M. Aghasibeig, H. Monajatizadeh, P. Bocher, A. Dolatabadi, R. Wuthrich, C. Moreau, Cold spray as a novel method for development of nickel electrode coatings for hydrogen production, Int J. Hydrog. Energy 41 (1) (Jan. 2016) 227–238, https://doi.org/10.1016/j.ijhydene.2015.09.123.

[19] W. Li, B. Yu, J. Tam, J.D. Giallonardo, D. Doyle, D. Poirier, J.G. Legoux, P. Lin, G. Palumbo, U. Erb, Microstructural characterization of copper coatings in development for application to used nuclear fuel containers, J. Nucl. Mater. 532 (Apr. 2020) 152039, https://doi.org/10.1016/j.jnucmat.2020.152039.

[20] A. Guitar, G. Vigna, M.I. Luppo, Microstructure and tensile properties after thermohydrogen processing of Ti–6Al–4V, J. Mech. Behav. Biomed. Mater. 2 (2) (Apr. 2009) 156–163, https://doi.org/10.1016/j.jmbbm.2008.06.002.

[21] M. Dunstan, B. Butler, I. Nault, J. Paramore, Effect Of Hydrogen Heat Treatment Of Cold Spray Additively Manufactured Ti-6Al-4V. in *World PM2022 Proceedings*, EPMA, Sep. 2022, https://doi.org/10.59499/wp225365785.

[22] A. Hamrani, A. Medarametla, D. John, A. Agarwal, Machine-Learning-Driven Optimization of Cold Spray Process Parameters: Robust Inverse Analysis for Higher Deposition Efficiency, Coatings 15 (1) (Dec. 2024) 12, https://doi.org/10.3390/coatings15010012.

[23] D. Kong, D. Zhao, G. Zhu, X. Ni, L. Zhang, W. Wu, C. Man, Y. Zhou, C. Dong, B. Sun, Heat treatment effects on the hydrogen embrittlement of Ti6Al4V fabricated by laser beam powder bed fusion, Addit. Manuf. 50 (Feb. 2022) 102580, https://doi.org/10.1016/j.addma.2021.102580.

[24] P. Metalnikov, D. Eliezer, G. Ben-Hamu, E. Tal-Gutelmacher, Y. Gelbstein, C. Munteanu, Hydrogen embrittlement of electron beam melted Ti–6Al–4V, J. Mater. Res. Technol. 9 (6) (Nov. 2020) 16126–16134, https://doi.org/10.1016/j.jmrt.2020.11.073.

[25] Z. Kacenka, M. Roudnicka, O. Ekrt, D. Vojtech, High susceptibility of 3D-printed Ti-6Al-4V alloy to hydrogen trapping and embrittlement, Mater. Lett. 301 (Oct. 2021) 130334, https://doi.org/10.1016/j.matlet.2021.130334.

[26] M. Ichimura, Y. Sasajima, M. Imabayashi, Grain Boundary Effect on Diffusion of Hydrogen in Pure Aluminum, Mater. Trans., JIM 32 (12) (1991) 1109–1114, https://doi.org/10.2320/matertrans1989.32.1109.

[27] A. Oudriss, J. Creus, J. Bouhattate, E. Conforto, C. Berziou, C. Savall, X. Feaugas, Grain size and grain-boundary effects on diffusion and trapping of hydrogen in pure nickel, Acta Mater. 60 (19) (Nov. 2012) 6814–6828, https://doi.org/10.1016/j.actamat.2012.09.004.

[28] A. Oudriss, S. Le Guernic, Z. Wang, B. Osman Hoch, J. Bouhattate, E. Conforto, Z. Zhu, D.S. Li, X. Feaugas, Meso-scale anisotropic hydrogen segregation near grain-boundaries in polycrystalline nickel characterized by EBSD/SIMS, Mater. Lett. 165 (Feb. 2016) 217–222, https://doi.org/10.1016/j.matlet.2015.12.016.

[29] J. Sayet, B.O. Hoch, A. Oudriss, J. Bouhattate, X. Feaugas, Multi-scale approach to hydrogen diffusion in FCC polycrystalline structure with binary classification of grain boundaries in continuum model, Mater. Today Commun. 34 (Mar. 2023) 105021, https://doi.org/10.1016/j.mtcomm.2022.105021.

[30] C.W. Adair, O.K. Johnson, Characterizing grain boundary network length features through a harmonic representation, Mater. (Oxf.) 35 (Jun. 2024) 102121, https://doi.org/10.1016/j.mtla.2024.102121.

[31] V. Randle, G.S. Rohrer, H.M. Miller, M. Coleman, G.T. Owen, Five-parameter grain boundary distribution of commercially grain boundary engineered nickel and copper, Acta Mater. 56 (10) (Jun. 2008) 2363–2373, https://doi.org/10.1016/j.actamat.2008.01.039.

[32] N. Yazdipour, A.J. Haq, K. Muzaka, E.V. Pereloma, 2D modelling of the effect of grain size on hydrogen diffusion in X70 steel, Comput. Mater. Sci. 56 (Apr. 2012) 49–57, https://doi.org/10.1016/j.commatsci.2012.01.003.

[33] E. Hanson, W.B. Andrews, M. Powers, K.G. Jenkins, K. Thornton, Simulating hindered grain boundary diffusion using the smoothed boundary method, Model Simul. Mat. Sci. Eng. 32 (5) (Jul. 2024) 055027, https://doi.org/10.1088/1361-651x/ad4d0b.

[34] L.I. Perez-Andrade, V.S. Bhattiprolu, W.M. Schuette, L.N. Brewer, Influence of powder properties and processing gas on the microstructural evolution of Armstrong CP-titanium and Ti6Al4V powders processed by cold spray, Surf. Coat. Technol. 431 (Feb. 2022) 128011, https://doi.org/10.1016/j.surfcoat.2021.128011.

[35] D. Porter, K. Easterling, M. Sherif, Crystal Interfaces and Microstructure. in *Phase Transformations in Metals and Alloys*, 3rd ed., CRC Press, Boca Raton, FL, 2009, pp. 115–188, ch. 3.

[36] C.A. Schneider, W.S. Rasband, K.W. Eliceiri, NIH Image to ImageJ: 25 years of image analysis, Nat. Methods 9 (7) (Jul. 2012) 671–675, https://doi.org/10.1038/nmeth.2089.

[37] J. Ma, "Im2mesh (2D image to triangular meshes)," MATLAB Central File Exchange. Accessed: Oct. 09, 2024. [Online]. Available: 〈https://www.mathworks.com/matlabcentral/fileexchange/71772-im2mesh-2d-image-to-triangular-meshes〉.

[38] S. Yin, N. Fan, C. Huang, Y. Xie, C. Zhang, R. Lupoi, W. Li, Towards high-strength cold spray additive manufactured metals: Methods, mechanisms, and properties, J. Mater. Sci. Technol. 170 (Jan. 2024) 47–64, https://doi.org/10.1016/j.jmst.2023.05.047.

[39] ABAQUS Inc, "Hydrogen diffusion in a vessel wall section," ABAQUS Example Problems Manual. Accessed: Oct. 17, 2024. [Online]. Available: 〈https://classes.engineering.wustl.edu/2009/spring/mase5513/abaqus/docs/v6.6/books/exa/default.htm?startat=ch07s01aex111.html〉.

[40] ABAQUS Inc, "Mass diffusion analysis," ABAQUS Analysis User's Manual. Accessed: Oct. 17, 2024. [Online]. Available: 〈https://classes.engineering.wustl.edu/2009/spring/mase5513/abaqus/docs/v6.6/books/usb/default.htm?startat=pt03ch06s08at25.html#usb-anl-amassdiffusion〉.

[41] ABAQUS Inc, "Mass diffusion analysis," ABAQUS Theory Manual. Accessed: Oct. 17, 2024. [Online]. Available: 〈https://classes.engineering.wustl.edu/2009/sprin

g/mase5513/abaqus/docs/v6.6/books/stm/default.htm?startat=ch02s13ath49.html#stm-anl-massdiffusion⟩.

[42] C.I. Steefel, K. Maher, Fluid-Rock Interaction: A Reactive Transport Approach, Rev. Miner. Geochem 70 (1) (Jan. 2009) 485–532, https://doi.org/10.2138/rmg.2009.70.11.

[43] M. Buchely, "Manual grain size measurement tool," MATLAB Central File Exchange. Accessed: Mar. 08, 2025. [Online]. Available: ⟨https://ww2.mathworks.cn/matlabcentral/fileexchange/162466-manual-grain-size-measurement-tool⟩.

[44] M. Hayoun, N. Eliaz, N.U. Navi, N. Lulu-Bitton, P. Shekhter, E. Sabatani, Electrochemical hydrogen permeation in wrought and electron beam melted Ti-6Al-4V alloys, Corros. Sci. 227 (Feb. 2024) 111760, https://doi.org/10.1016/j.corsci.2023.111760.

[45] S. Huang, H. Li, H. Zhang, J. Sheng, E. Agyenim-Boateng, J. Lu, Experimental study and finite element simulation of hydrogen permeation resistance of Ti-6Al-4V alloy strengthened by laser peening, Surf. Coat. Technol. 400 (Oct. 2020) 126217, https://doi.org/10.1016/j.surfcoat.2020.126217.

[46] S.G. MacLeod, D. Errandonea, G.A. Cox, H. Cynn, D. Daisenberger, S.E. Finnegan, M.I. McMahon, K.A. Munro, C. Popescu, C.V. Storm, The phase diagram of Ti-6Al-4V at high-pressures and high-temperatures, J. Phys.: Condens. Matter 33 (15) (Apr. 2021) 154001, https://doi.org/10.1088/1361-648X/abdffa.

[47] L.C. Liu, H.R. Gong, Hydrogen solubility and diffusivity at Σ3 grain boundary of PdCu, RSC Adv. 11 (22) (2021) 13644–13652, https://doi.org/10.1039/d0ra10133h.

[48] R.B. Bird, W.E. Stewart, E.N. Lightfoot, Concentration Distributions in Solids and Laminar Flow (Ed), in: W. Anderson (Ed.), in *Transport Phenomena*, 2nd, Wiley, New York, NY, 2007, pp. 543–581 (Ed).

[49] V. Ardourel, J. Jebeile, On the presumed superiority of analytical solutions over numerical methods, Eur. J. Philos. Sci. 7 (2) (May 2017) 201–220, https://doi.org/10.1007/s13194-016-0152-2.

[50] E. Vasikaran, Y. Charles, P. Gilormini, Implementation of a reaction-diffusion process in the Abaqus finite element software, Mech. Ind. 21 (5) (Aug. 2020) 508, https://doi.org/10.1051/meca/2020010.

[51] A.M. Brass, A. Chanfreau, Accelerated diffusion of hydrogen along grain boundaries in nickel, Acta Mater. 44 (9) (Sep. 1996) 3823–3831, https://doi.org/10.1016/1359-6454(95)00446-7.

[52] M.D. Dolan, Non-Pd BCC alloy membranes for industrial hydrogen separation, J. Memb. Sci. 362 (1–2) (Oct. 2010) 12–28, https://doi.org/10.1016/j.memsci.2010.06.068.

[53] K. Xu, Hydrogen embrittlement of carbon steels and their welds. in *Gaseous Hydrogen Embrittlement of Materials in Energy Technologies*, Elsevier, 2012, pp. 526–561, https://doi.org/10.1533/9780857093899.3.526.

[54] T. Liu, M.D. Vaudin, J.R. Bunn, T. Ungár, L.N. Brewer, Quantifying dislocation density in Al-Cu coatings produced by cold spray deposition, Acta Mater. 193 (Jul. 2020) 115–124, https://doi.org/10.1016/j.actamat.2020.04.040.

[55] S. Msolli, Z.-Q. Zhang, D.H.L. Seng, Z. Zhang, J. Guo, C.D. Reddy, N. Sridhar, J. Pan, B.H. Tan, Q. Loi, An experimentally validated dislocation density based computational framework for predicting microstructural evolution in cold spray process, Int J. Solids Struct. 225 (Aug. 2021) 111065, https://doi.org/10.1016/j.ijsolstr.2021.111065.

[56] Y.-K. Kim, H.-J. Kim, K.-A. Lee, Solid-state cold spray additive manufacturing of pure tantalum with extraordinary high-temperature mechanical properties, J. Mater. Res. Technol. 23 (Mar. 2023) 5698–5709, https://doi.org/10.1016/j.jmrt.2023.02.184.

[57] G. Liu, K. Leng, X. He, L. Tang, W. Gao, Y. Fu, Microstructure evolution of Ti–6Al–4V under cold rolling + low temperature nitriding process, Prog. Nat. Sci.: Mater. Int. 32 (4) (Aug. 2022) 424–432, https://doi.org/10.1016/j.pnsc.2022.06.004.

[58] S. Kerealme Yeshanew, C. Bai, Q. Jia, T. Xi, Z. Zhang, D. Li, Z. Xia, R. Yang, K. Yang, Microstructure evolution, tensile properties and internal structure transformation study on Ti6Al4V–5Cu anti-bacterial alloy during uniaxial tensile straining at low forming temperature, Mater. Chem. Phys. 298 (Apr. 2023) 127478, https://doi.org/10.1016/j.matchemphys.2023.127478.

[59] A. Oudriss, J. Creus, J. Bouhattate, C. Savall, B. Peraudeau, X. Feaugas, The diffusion and trapping of hydrogen along the grain boundaries in polycrystalline nickel, Scr. Mater. 66 (1) (Jan. 2012) 37–40, https://doi.org/10.1016/j.scriptamat.2011.09.036.

[60] T. Awane, The method of removing hardly soluble organic material from metallic specimen used in fracture surface analysis by scanning electron microscope, Microscopy 62 (6) (Dec. 2013) 615–621, https://doi.org/10.1093/jmicro/dft025.

[61] B. Murgas, J. Stickel, S. Ghosh, Generative adversarial network (GAN) enabled Statistically equivalent virtual microstructures (SEVM) for modeling cold spray formed bimodal polycrystals, NPJ Comput. Mater. 10 (1) (Feb. 2024) 32, https://doi.org/10.1038/s41524-024-01219-4.